iScience

CellPress
OPEN ACCESS

Article

# Mechanism of local electric oxidation on two-dimensional $MoS_2$ for resistive memory application

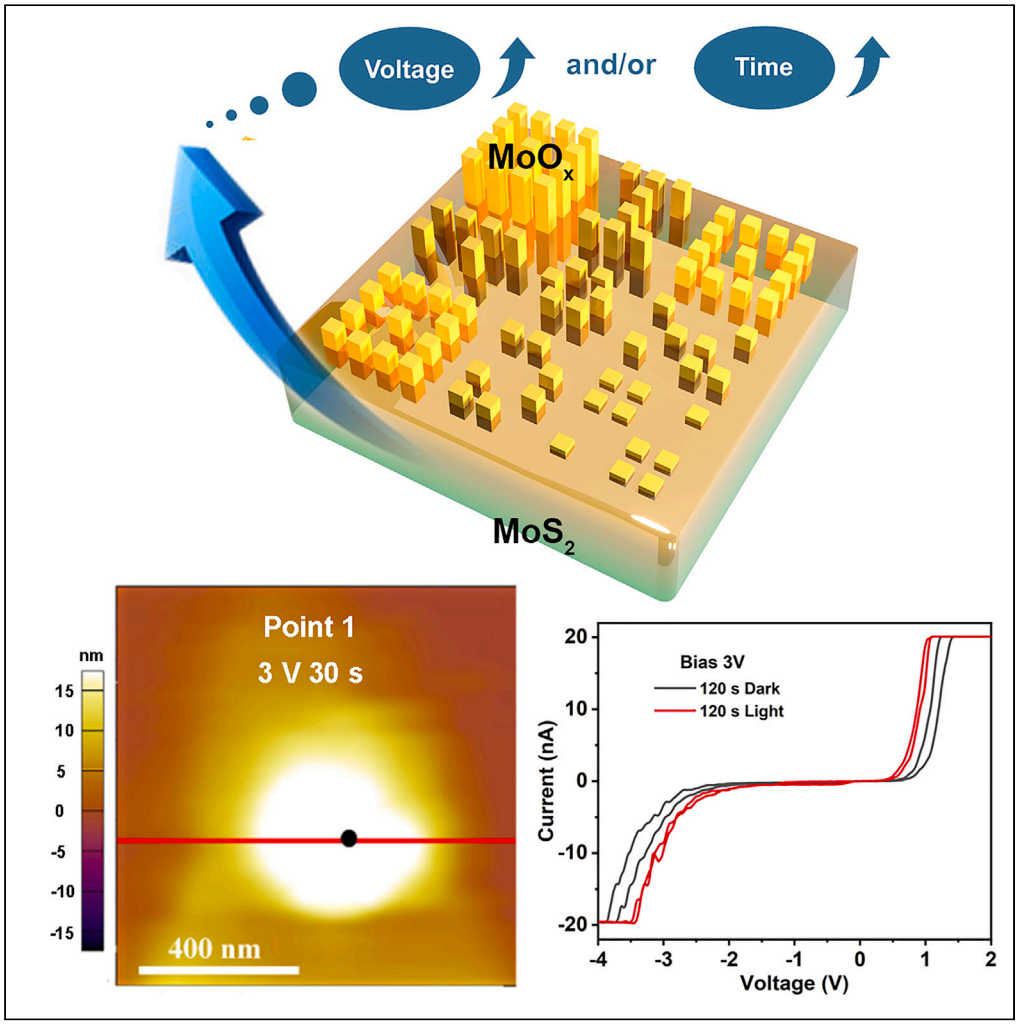


Hui Dong, Junzheng Mu, Jinfeng Peng, Xuejun Zheng, Liang Chu

zhengxuejun@xtu.edu.cn (X.Z.)
chuliang@hdu.edu.cn (L.C.)

## Highlights

$MoS_2$-$MoO_3$ local heterojunctions are constructed via local electric oxidation

Novel thermal oxidation model is proposed to understand local electric oxidation

Multi-state memory storage is realized by local heterojunctions at the nanoscale

Photoelectric cooperative nano quick response code are suggested

Dong et al., iScience 27, 110819
October 18, 2024 
https://doi.org/10.1016/j.isci.2024.110819

iScience

CellPress
OPEN ACCESS

Article

# Mechanism of local electric oxidation on two-dimensional $MoS_2$ for resistive memory application

Hui Dong,[1] Junzheng Mu,[3] Jinfeng Peng,[3] Xuejun Zheng,[1,*] and Liang Chu[2,4,*]

## SUMMARY

**The manipulation and mechanism of two-dimensional (2D) transition metal dichalcogenides (TMDs) by external electric field are significant to the photoelectric properties. Herein, the 2D $MoS_2$ nanosheets were oxidized to form $MoS_2$-$MoO_3$ local heterojunctions by an electric field, applied in multistable memristors for the proposal of NanoQR code. A modified thermal oxidation model was derived to reveal the mechanism of local electric oxidation on 2D $MoS_2$. From current-voltage curves, the barrier height of the $MoS_2$ device showed an increase of 0.39 eV due to local oxidation after applying voltage for 480 s. Based on density-functional theory, the increase of barrier height was calculated as 0.38 eV between $MoS_2$-$MoS_2$ and $MoS_2$-$MoO_3$ supercells. The 2D $MoS_2$-$MoO_3$ local heterojunctions were further applied as multistable memory storage at the nanoscale. The findings suggest a novel strategy for controlling local electric oxidation on 2D TMDs to manipulate the properties for the application of photoelectric memory nanodevices.**

## INTRODUCTION

Two-dimensional (2D) transition metal dichalcogenides (TMDs, e.g., $WSe_2$, $WS_2$, and $MoTe_2$) have been considered of great interest due to their excellent photoelectric properties of the unique valley-polarized optical response, fast photoresponse speed and high absorption for photoelectric applications.[1,2] However, oxidation has been generally regarded as the primary fault for the long-term stability of TMD-based nanodevices.[3] Particularly, the stability of mono and a few-layer 2D TMDs is of vital importance due to the layer-dependent properties.[4] For example, the $MoO_3$ surface causes a large band offset with the buried $MoS_2$ due to the different band structures from density-functional theory (DFT).[5] In an oxygen (air) environment, the surface of 2D TMDs would be oxidized under an electric field, and their devices are severely degraded in terms of current level, carrier concentration, and carrier mobility.[6,7] In order to avoid oxidation, the oxygen-free environment must be selected to measure the long-term stable TMD-based devices in the laboratory,[8] and the device packaging is a prerequisite to realize long-term operation with high stability in practical applications.[9]

The chemical reaction occurs more rapidly with increasing temperature because more activated molecules collide vigorously, which increases the probability of bond cleavage and rearrangement.[10,11] In the low dimensional systems, there are nanoscale hot spots, which are difficult to dissipate heat and easily cause the device failure from overheating.[12,13] The thermal oxidation of TMDs has been investigated by *in-situ* Raman spectra over a wide range of temperatures.[14] The $WS_2$ monolayer will be oxidized when it is exposed to the ambient condition with the presence of light.[15] The in-situ-grown $WS_2$ monolayer on suspended graphene can resist oxidation because of the screening effect from the conductive graphene substrate, while the $WS_2$ on the $SiO_2$ substrate would be easily oxidized. In other words, the controlled layer-by-layer oxidation on TMDs could be significant in constructing 2D heterojunctions for advanced photoelectric devices. Previously, the whole surface of $MoTe_2$ nanosheets was oxidized to MoOx with atomic-level accuracy by varying ozone exposure time, which were further integrated into complementary metal oxide semiconductor (CMOS) devices.[16] Notably, the electric field can accelerate the charge carriers to generate more Joule energy, which can also induce chemical reactions. Thus, the local oxidation of $WS_2$ on the $SiO_2$ substrate can be created by a local electric field using a conductive atomic force microscope (AFM).[17] In previous studies, the local oxidation on the TMD surface has been observed with an AFM tip. However, the oxidation mechanism has been needed to deeply analyze for guiding possible practical applications.[18,19]

To date, memory devices are desired to simultaneously meet the demands of high storage density, non-volatility, fast operation, and low power consumption. To achieve high storage density, there are typically two paths in principle: minimizing effective cells and developing

[1]School of Electro-mechanical Engineering, Guangdong University of Technology, Guangzhou 510006, China
[2]School of Electronics and Information & Institute of Carbon Neutrality and New Energy, Hangzhou Dianzi University, Hangzhou 310018, China
[3]School of Mechanical Engineering & Engineering Research Center of Complex Tracks Processing Technology and Equipment of MoE & Key Laboratory of Welding Robot and Application Technology of Hunan Province, Xiangtan University, Xiangtan 411105, China
[4]Lead contact
*Correspondence: zhengxuejun@xtu.edu.cn (X.Z.), chuliang@hdu.edu.cn (L.C.)
https://doi.org/10.1016/j.isci.2024.110819

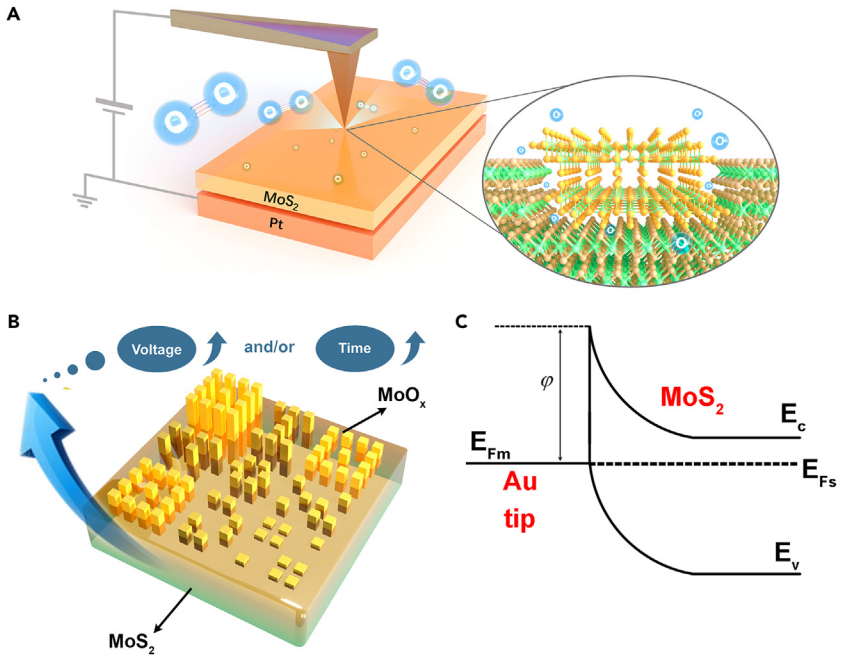


**Figure 1. Schematic diagram of device structure and NanoQR code**

(A) 2D $MoS_2$-based nanodevice with C-AFM top electrode, where the local electric oxidation can construct local $MoS_2$-$MoO_3$ heterostructures.

(B) Thickness of local $MoS_2$-$MoO_3$ heterostructures can be tuned by various voltages at different times. The heterostructure array can be used as NanoQR code.

(C) Schematic diagram of the barrier height of 2D $MoS_2$-based nanodevice with C-AFM top electrode.

multistate storage.[20,21] The multistate memory technique can increase the storage density beyond Von Neumann's architecture.[22] The storage cell miniaturization can increase the density of memory, accompanied by the decrease of cost per bit at the nanoscale.[23] Memristor has been regarded as the most potential non-volatile resistance memory because of the simple structure, fast read and write, high integration, and nanoscale.[24] In recent years, it is expected to realize the multi-state resistance properties based on photo-responsive semiconductors via the cooperative regulation of both light and electric fields.

Herein, the photoelectric properties of 2D $MoS_2$ nanosheets were manipulated to form $MoS_2$-$MoO_3$ local heterostructures by local electic oxidation from AFM tip, which can be further applied in light-assisted multistate memristors for NanoQR code information. The local electric field from the AFM tip can simultaneously construct and tune memories at the nanoscale. Based on the finite-element method (FEM) simulation, a modified thermal oxidation model was proposed by introducing Ohmic dissipation to describe the dependence of oxidation thickness on the applied voltage with loading time. The current-voltage (I-V) and current-time (I-T) characteristics were measured by the applied voltage for the different loading time intervals. The experimental barrier height difference between $MoS_2$-$MoS_2$ and $MoS_2$-$MoO_3$ was calculated from the *I-V* curves through Fowler–Nordheim tunneling (FNT) theory, which consists with the value by DFT based on the atomic supercell models. The different barrier height decline is caused by the formation of $MoO_3$ with different thicknesses under the local applied voltage, which can represent different light-assisted multistate memristors for NanoQR code information application. Thus, the utilization of the local electric oxidation of 2D TMDs (usually detrimental) provides a new principle and novel way for the design of photoelectric nanodevices.

## RESULTS AND DISCUSSION

The 2D $MoS_2$-based nanodevice with AFM-top electrode was schematically depicted in Figure 1A. The $MoS_2$-based nanodevice was constructed as Au tip/$MoS_2$ nanosheet/Pt substrate, and then the voltage was applied. It is notable that under an electric field in air condition, the $MoO_3$ local surfaces are formed on the $MoS_2$ nanosheet to construct 2D heterostructures. The local thickness of the nanosheet increases under the applied voltage due to the formation of $MoO_3$ local surface. The oxidation aroused by the local electrical field would change the barrier height, which has a great effect on the photoelectric performance of the constructed nanodevices. On one hand, the relative thicknesses of $MoS_2$-$MoO_3$ heterostructures can be changed by applying voltage with different loading times (Figure 1B). The oxidation thickness increases with the applied voltage and loading time, which leads to different memory states. Importantly, the precisely controlled local 2D heterojunction memristors can realize information confidential storage, because of the 2D bar code characteristics at the nanoscale. On the other hand, every local $MoS_2$-$MoO_3$ heterostructure can realize the characteristic of resistive random access memory. Because the effective contact is the effective emission area at the injecting electrode of the Au tip and the corresponding barrier height refers to the barrier between the Fermi level of the Au tip and the bottom of the conduction band $MoS_2$ or $MoO_3$-$MoS_2$ according to Fowler-Nordheim tunneling theory

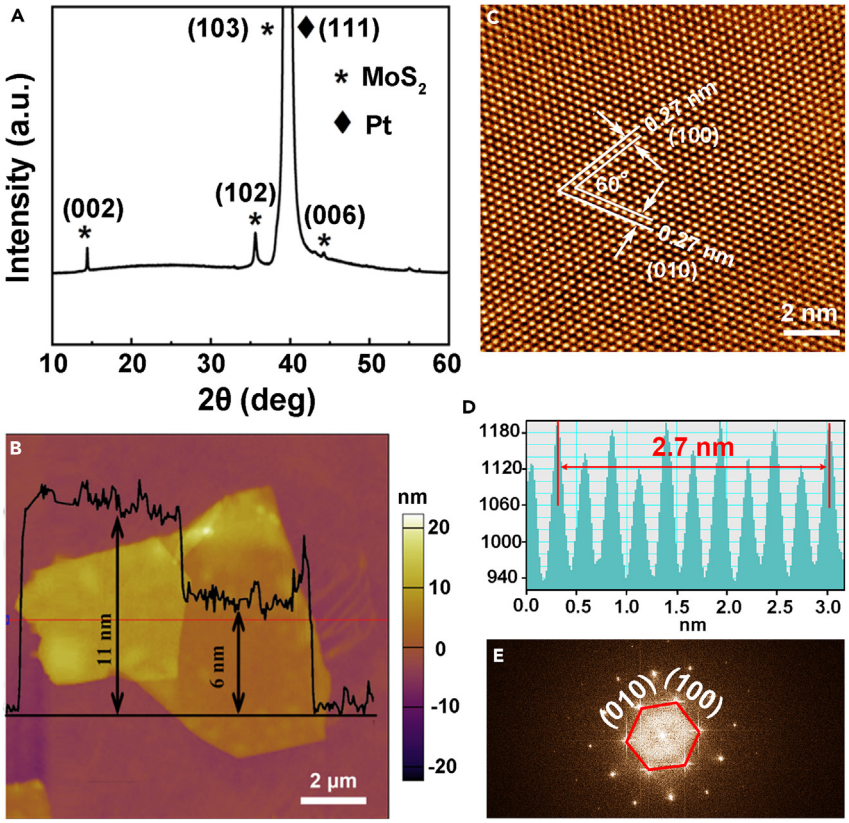


**Figure 2. Characterization of $MoS_2$ nanosheet**

(A) XRD pattern, (B) AFM image, (C) HRTEM, (D) intensity profile extracted from (C), (E) corresponding FFT image.

(Figure 1C).[25] Thus, we proposed information NanoQR code with strong encryption for the first time, in which every cell is a distinctive multi-state photoelectric memristor.

X-ray diffraction (XRD) pattern of the $MoS_2$ nanosheet on Pt/$SiO_2$/Si substrate is recorded as Figure 2A. The strongest peak at 40° can be indexed to the Pt phase (JCPDS No. 04–0802), and the others could be assigned to the hexagonal $MoS_2$ phase with the lattice parameters of $a = b = 0.31612$ nm and $c = 1.22985$ nm (JCPDS No. 37–1492). No impurity phases can be detected in the pattern, indicating the pure $MoS_2$ phase. Energy dispersive X-ray (EDX, installed on SEM equipment) spectroscopy further confirmed the pure $MoS_2$ initially (Figure S1). AFM technology was carried out to illustrate the prepared $MoS_2$ nanosheet in Figure 2B. There are obvious hierarchical structures with thicknesses of 6 and 11 nm, indicating the multilayer nanosheet. The HRTEM image of the $MoS_2$ nanosheet indicates a single-crystal characteristic in Figure 2C. The face angle of 60° shows the hexagonally symmetric lattice structure of the $MoS_2$ nanosheet. The lattice spacing is estimated as 0.27 nm, which corresponds to the (100) or (010) plane of $MoS_2$. The intensity profile further conformed to the lattice spacing of 0.27 nm in Figure 2D. The fast Fourier transformation (FFT) pattern are plotted in Figure 2E, which also indicates the single-crystalline characteristics with the hexagon indexed to the (010) and (110) planes of hexagonal-phase $MoS_2$.

The points marked as "1," "2," and "3" were selected to apply voltage on the $MoS_2$ nanosheet with the pristine height of ~11 nm, and their AFM images at the pristine states are indicated in Figures 3A–3C, respectively. The voltages of 3, 4, and 5 V were applied for 30 s at the "1," "2," and "3" points, and the corresponding AFM images are illustrated in Figures 3D–3F, respectively. Obviously, the thicknesses of "1," "2," and "3" points increase remarkably after applying the voltages. The cross-sections before and after applying voltage are indicated in Figures 3G–3I. The thicknesses increased from the pristine height of 11.0–25.1, 31.4, and 68.7 nm, and the corresponding height variations are 14.1, 20.4, and 57.7 nm for the "1," "2," and "3" points, respectively. The height variations of the devices under 3, 4, and 5 V for 30 s are 1, 2, and 1 nm, respectively from Figure 3. As compared with height variations of 14.1, 20.4, and 57.7 nm, the oxidation error is located at the error of 10%. Similarly, 0.1, 0.3, and 0.5 V with the loading time interval of 480 s were applied at the points "4," "5," and "6." The pristine height is 6 nm as shown in Figures S2A–S2C, and the thickness variations are found to be 13.2, 19.8, and 24.9 nm, respectively. The relationship between oxidation thickness and rate with time and voltage is summarized in Table 1. The oxidation thickness increases with applied voltage at a certain time of 30 and 480 s and the oxidation rate is also in in proportion with voltage independence of position, which indicates that the voltage could be utilized as a simple method to control oxidation thickness and rate precisely at the nanoscale. The local thickness increase can be ascribed to local oxidation reaction under the electric field.

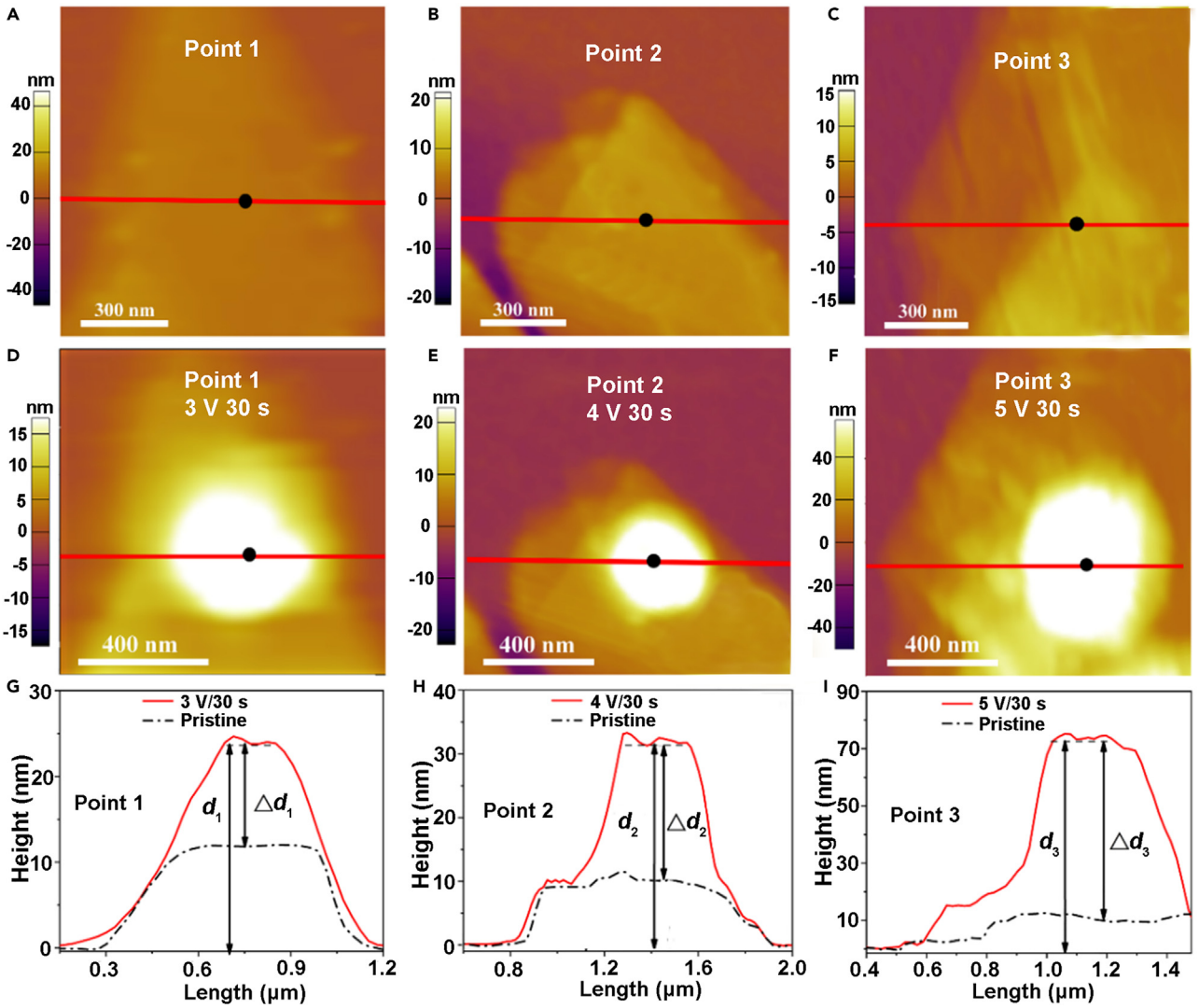


**Figure 3. AFM images of $MoS_2$ nanosheets before and after applying voltage**

(A–C) Points "1," "2," and "3" at the pristine states and (D–F) after applying a voltage of 3, 4, and 5 V with a time interval of 30 s.

(G–I) The corresponding cross-sections with different increasing heights.

To further understand the morphological changes in the $MoS_2$ vertical heterostructure, a high-resolution transmission electron microscope (HRTEM) and Energy dispersive spectrometer (EDS) are used to characterize its structural distortion under the applied voltage of 3 V. After the formation of four hillocks set by the cyclic electrical field on the surface of the $MoS_2$ heterostructure (Figure 4A), a focused ion beam (FIB) was performed to cut along the red line to obtain the cross-section (Figure 4B) for TEM characterization. An energy dispersive spectrometer (EDS) was used to characterize the respective I and II regions marked by a yellow rectangle, and the corresponding results were summarized in

**Table 1. Relationship between oxidation thickness and rate with time and voltage**

| Time (s) | Voltage(V) | Oxidation thickness(nm) | Oxidation rate (nm/s) |
|---|---|---|---|
| 30 | 3 | 25.1 | 0.84 |
| 30 | 4 | 31.4 | 1.05 |
| 30 | 5 | 68.7 | 2.29 |
| 480 | 0.1 | 13.2 | 0.03 |
| 480 | 0.3 | 19.8 | 0.04 |
| 480 | 0.5 | 24.9 | 0.05 |

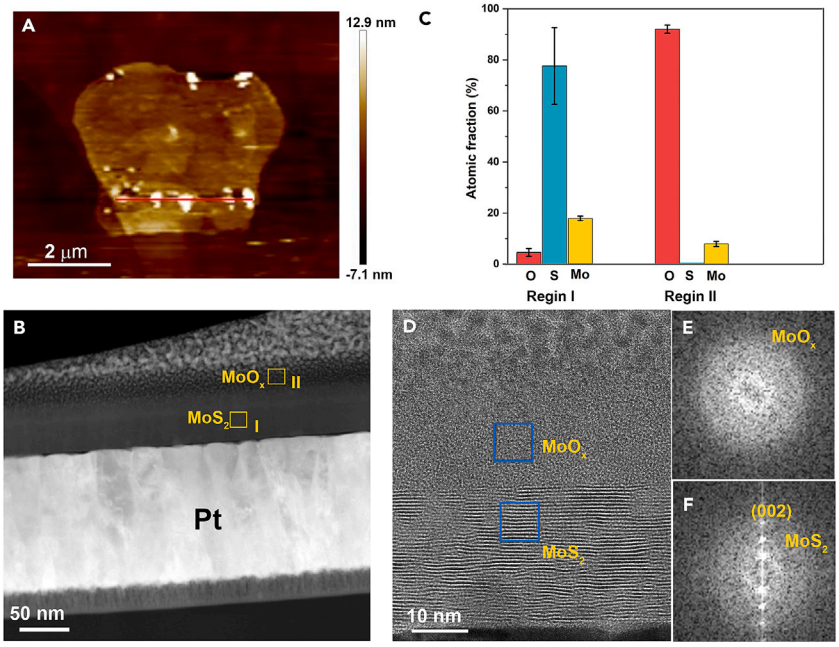


**Figure 4. $MoS_2$-$MoO_3$ heterostructure characterization**

(A) AFM image of four hillocks formed on the surface of $MoS_2$.

(B) Cross-sectional TEM image processed along with the position and direction of the red line in (A) by the FIB.

(C) Atomic fraction of Regin I of $MoS_2$ and regin II of MoOx marked by the yellow rectangle in (B). HRTEM image of the cross-section of $MoO_x$/$MoS_2$ heterostructure.

(D) and the corresponding fast Fourier transform pattern of $MoO_x$ (E) and $MoS_2$ in (F).

Figure 4C. Oxygen only occupied less than five in region I while rising up to 90% in region II after voltage was applied, indicating that the oxidation process was induced by the AFM tip under the electric field. More efforts have been made with HRTEM and related fast Fourier transform to elucidate the structural modifications of the heterostructure after voltage application. As shown in Figures 4D and 4F, the single-crystal $MoS_2$ has a d-spacing of 6.3 Å, corresponding to the (002) plane. However, it is difficult to distinguish the crystal structures of the molybdenum oxide layer due to its amorphization (Figures 4D and 4E). In conclusion, the formation of a molybdenum oxide layer under the local electric field was further confirmed by both EDS and HRTEM analyses.

In order to further confirm the local oxidation reaction, Raman spectra were carried out to investigate the $MoS_2$ nanosheet before and after applying a local voltage of 5 V for 30 s (Figure 5A). There are the peaks of $E^1_{2g}$ at 384 $cm^{-1}$ and $A_{1g}$ at 407 $cm^{-1}$ with several peaks of the weak intensity for the second-order and combination phonon modes. The primary Raman active modes ($E^1_{2g}$ and $A_{1g}$) are corresponded to $MoS_2$.[26,27] After applying the voltage, the peak intensity of $E^1_{2g}$ and $A_{1g}$ is found to be similar to the initial states.[28] The enlarged peaks of (i), (ii), and (iii) at the Raman shifts (Figure 5B) show the two main peaks appear at 820 $cm^{-1}$ (i) and at 954 $cm^{-1}$ (ii), indicating the formation of $MoO_3$[29] and $MoO_{3-x}$.[30] One peak (iii) with very weak intensity appears at 820 $cm^{-1}$, which indicates the oxygen chemisorption on the surface of the $MoS_2$ nanosheet due to the active surface defects at a pristine state. After applying the voltage, the peak intensity at the Raman shift (820 $cm^{-1}$) of the local $MoS_2$ nanosheet is much larger than that of the original $MoS_2$ nanosheet, and the former peak area fitted after baseline subtraction is found to be 371% larger than that of the latter. The increased peak "i" and additional peak "ii" confirm the formed local oxide surface on the $MoS_2$ nanosheet under the applied voltage.

The thickness variation can be defined as a function of the applied voltage, as shown in Figure 5C for points "1," "2," and "3" and Figure 5D for points"4," "5," and "6," Obviously, the thickness variations at the points "1," "2," and "3" increase with the applied voltage. Thus, it can be concluded that the thickness variations from the AFM profiles in Figures 2 and S2 are identified as the thickness of $MoO_3$ based on Raman spectra analysis in Figure 5B. The thermal oxidation model has already been successfully utilized to describe the thickness variation of the oxidation surface under the thermal field.[31] Thus the Joule heating as the thermal field can be introduced to describe the oxidation thickness variation. The formation mechanism of molybdenum oxide could be illustrated through the chemical equation: $2MoS_2+7O_2 \rightarrow 2MoO_3+4SO_2$. The chemical bonds of Mo-S were broken, and chemical bonds of Mo-O and S-O recombined under the Joule heating induced by voltage, therefore molybdenum oxide was formed with the chemical bonds of Mo-S destruction and Mo-O recombination. The oxidation thickness shows a linear relationship with the loading time according to the thermal oxidation model[31]:

$$\Delta d = k \times (t + \tau) \quad \text{(Equation 1)}$$

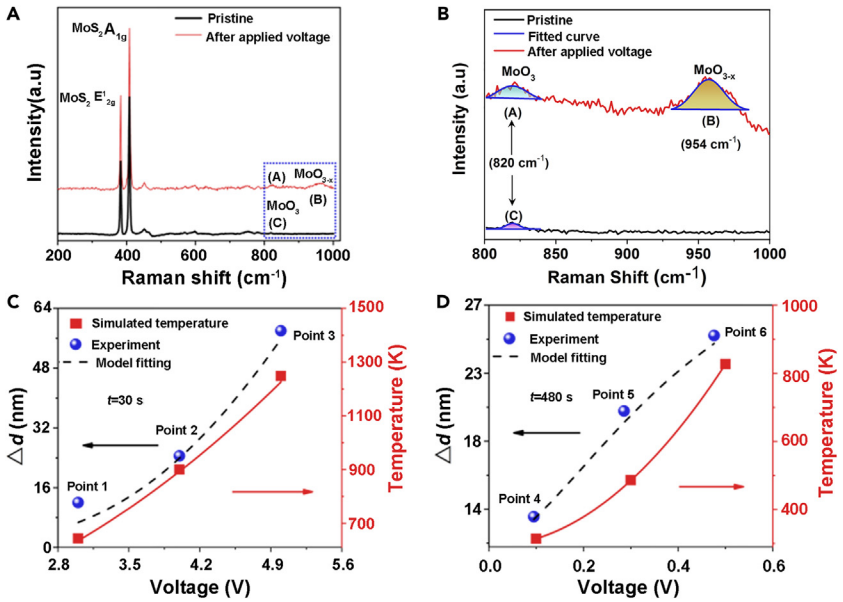


**Figure 5. $MoS_2$-$MoO_3$ heterostructure construction with thickness increasing after voltage loading**

(A) Raman spectra of $MoS_2$ nanosheet at the pristine state and after the applied voltage and (B) the enlarged peaks of (i), (ii), and (iii) from Raman spectra. The experimental thickness variation $\Delta d$ and the maximum temperature simulated by the FEM method as a function of the applied voltage (C) at the points "1," "2," and "3" in Figure 3 and (D) at the points "4," "5," and "6" in Figure S2.

where $t$ is the loading time interval, $\tau$ is the time constant, and $k$ is the oxidation rate of linearity. The influence of temperature on the chemical reaction rate is always interpreted in terms of the Arrhenius equation, and $k$ can be expressed as the following equation[32]:

$$k = A\exp\left(\frac{-E}{GT}\right) \quad \text{(Equation 2)}$$

where $A$ is the pre-exponential factor, $E$ is the activation energy, $T$ is the temperature, and $G$ is the gas constant.

To explore the temperature on the oxidation rate of linearity, FEM simulation was carried out to obtain the temperature distribution induced by the Joule heating, as shown in Figure 3 for the points "1," "2," "3" under 3, 4, 5 V, respectively, and Figure S3 for the points "4," "5," "6" under 0.1, 0.3, 0.5 V, respectively. The maximum temperature occurs at the applied voltage points on the local surface of $MoS_2$ nanosheets, which are summarized as the function of the applied voltage in Figures 5C and 5D. The maximum temperature of the local oxide surface can be fitted by the Ohmic dissipation model as depicted by the red lines[33]:

$$T = T_0 + \alpha\frac{-V^2}{R} \quad \text{(Equation 3)}$$

where $\alpha$ is the thermal resistance, $V$ is the applied voltage, $T_0$ is the room temperature, and $R$ is the resistance. The relationship between the thickness variation $\Delta d$ and the applied voltage $V$ can be expressed from the Equations 1, 2, and 3 as the following equation:

$$\Delta d = A\exp\left(\frac{-E}{G\left(T_0+\frac{\alpha V^2}{R}\right)}\right)\times(t+\tau) \quad \text{(Equation 4)}$$

The modified thermal oxidation model can fit the relationship between $\Delta d$ and $V$ at the different loading time intervals, which are marked by the black dashed lines in Figures 5C and 5D for 30 s and 480 s. Obviously, the experimental thickness variation is in good agreement with the modified model.[10] Therefore, the oxidation thickness variation on the $MoS_2$ nanosheet under the local applied voltage is dominated by the thermal oxidation due to the Joule heating. Herein, it is the first time to illuminate the mechanism on tuning atomic 2D heterojunction using the local electric field, which can offer novel guidelines to control the local oxidation with atomic precision.

The $I$-$V$ curves at the applied voltage of 0.5 V with different loading time intervals are demonstrated in Figure 6A for the $MoS_2$ nanosheet at point "6" in Figure S2C. The effective contact area $A_{eff}$ is estimated as ~$7.04 \times 10^{-16}$ $m^2$ according to the AFM tip with a diameter of 30 nm from Figure S5, and thus the $\ln(I/V^2)$ versus $1/V$ curves can be fitted by Equation 6 in the methodology, as shown in the inset of

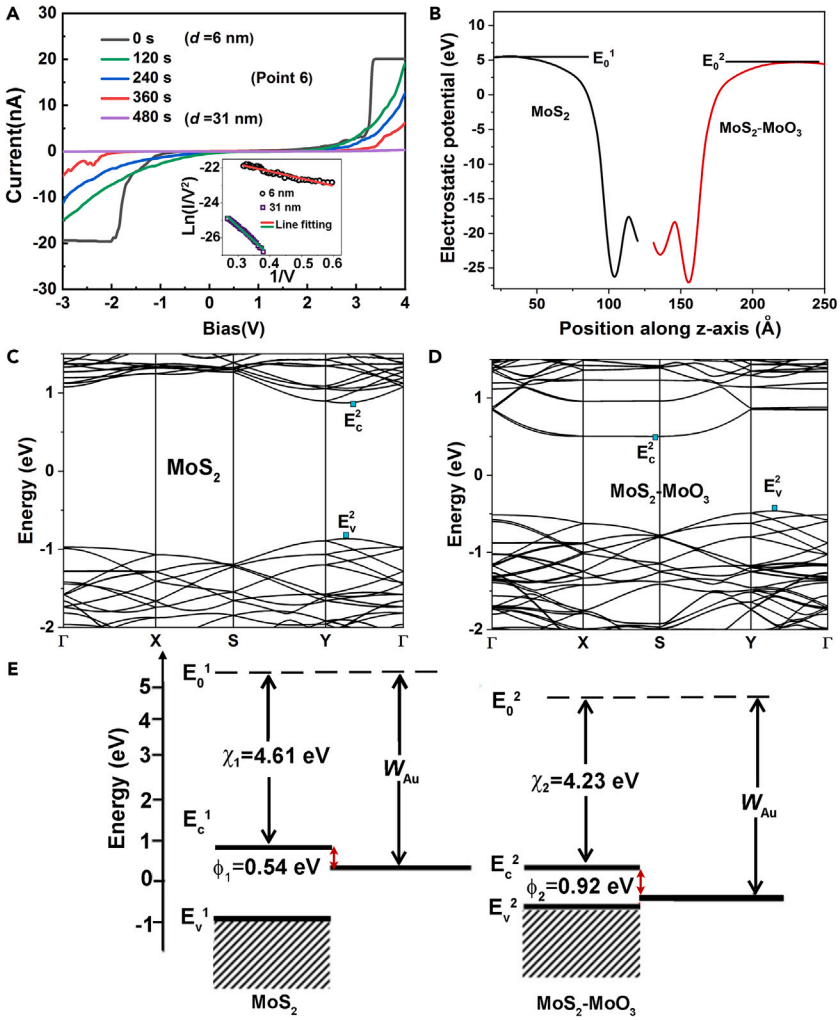


**Figure 6. Barrier height variation after constructing $MoS_2$-$MoO_3$ heterostructure**

(A) *I-V* curves of $MoS_2$ nanosheet at the point "6" with the different loading time intervals and $\ln(I/V^2)$ versus $1/V$ curves fitted by the FNT model for 6 and 31 nm in the inset.

(B) Calculated electrostatic potential as a function of the position along z axis of $MoS_2$-$MoS_2$ homostructure and $MoS_2$-$MoO_3$ heterostructure. Band structures for (C) $MoS_2$ homostructure and (D) $MoS_2$-$MoO_3$ heterostructure calculated by DFT.

(E) Energy level change of $MoS_2$ and $MoS_2$-$MoO_3$. The work function of gold ($W_{Au}$) is 5.15 eV.[35]

Figure 6A. There is a strong linear relationship between $\ln(I/V^2)$ and $1/V$, which indicates that the tunneling current through ultrathin $MoS_2$ and $MoS_2$-$MoO_3$ heterostructure can be explained by the FNT model. The barrier heights are fitted as 0.51 eV ($\phi_e^1$) for the $MoS_2$ nanosheet with a thickness of 6 nm, and 0.9 eV ($\phi_e^2$) for the $MoS_2$-$MoO_3$ heterostructure with a thickness of 31 nm. Therefore, the barrier height difference ($\Delta\phi_e = \phi_e^1 - \phi_e^2$) is 0.39 eV. The formation of $MoO_3$ induced by the applied voltage leads to an increase in barrier height. The vacuum level $E_0^1$ and the conduction band minimum $E_c^1$ for $MoS_2$, and $E_0^2$ and $E_c^2$ for $MoS_2$-$MoO_3$ heterostructure can be obtained by the DFT method.[34] And the variation of Schottky barrier height through Equations 3 and 4 can be explained by comparing with the experimental and simulation differences of the barrier height $\Delta\phi_e$. In order to calculate the variation of Schottky barrier height under the applied voltage, the atomic models of $MoS_2$-$MoS_2$ homostructure and $MoS_2$-$MoO_3$ heterostructure were constructed for the DFT calculation (Figure 6B). The $MoS_2$-$MoS_2$ homostructure and $MoS_2$-$MoO_3$ heterostructure represent the $MoS_2$ nanosheet in a pristine state and applied voltage state, respectively.

The electrostatic potentials of the $MoS_2$-$MoS_2$ and $MoS_2$-$MoO_3$ supercells are calculated as the functions of the distance along the z axis of the thickness (Figure 6B). As for the $MoS_2$-$MoS_2$ and $MoS_2$-$MoO_3$ supercells, the vacuum levels $E_0^1$ and $E_0^2$ are extracted as 5.48 and 4.73 eV, respectively. The band structures of the $MoS_2$-$MoS_2$ homostructure and $MoS_2$-$MoO_3$ heterostructure are presented in Figures 6C and 6D to obtain the corresponding $E_c^1$ and $E_c^2$, respectively. The conduction band minimum of $E_c^1$ and $E_c^2$ are extracted as 0.87 and 0.50 eV, respectively. The energy level difference between $MoS_2$ and $MoS_2$-$MoO_3$ supercells is schematically

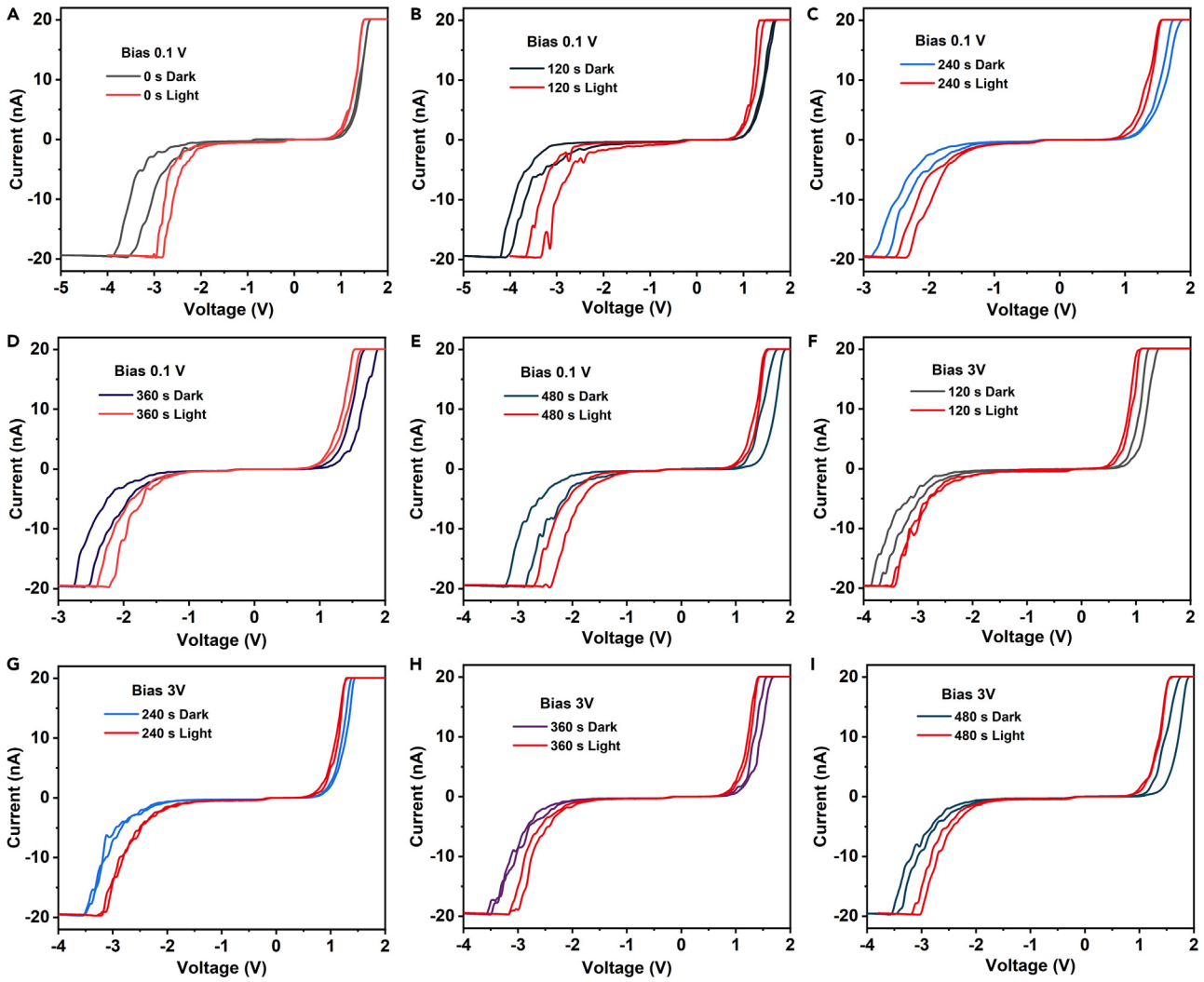


**Figure 7. Photoelectric properties with voltage and loading time interval on the resistance states**

*I*–*V* curves of the $MoS_2$-based nanodevice with time intervals of 0 s (A), after applied voltage of 0.1 V (B–E) and 3 V (F–I) under dark and light irritation with time intervals of 120, 240, 360, 480 s.

depicted in Figure 6E. Thus, it can be compared to the barrier height variation caused by the formation of $MoO_3$ under the locally applied voltage. The Schottky barrier heights of $\phi_1$ and $\phi_2$ are calculated as 0.54 and 0.92 eV for Au/$MoS_2$ and Au/$MoS_2$-$MoO_3$ heterostructure, respectively. Therefore, the simulation difference of barrier height $\Delta\phi$ (0.38 eV) approaches the experimental result $\Delta\phi_e$ (0.39 eV) from the inset of Figure 6A. Both the experimental and theoretical results confirm that the increase in height in the Schottky barrier of the $MoS_2$ nanosheet is caused by the formation of $MoO_3$ at the local applied voltage. The study can be helpful in understanding the degradation mechanism of the electrical performance, which will provide the safe working voltage and time of 2D material devices at the atomic scale.

In order to investigate the effect of voltage and loading time interval on the resistance states, we further carried current versus voltage (*I*–*V*) curves without and with light illustration after applying a voltage of 0.1 V at loading time intervals (Figures 7A–7E). All *I*–*V* curves show the bipolar conductive behaviors after the formation of conductive paths in the vertical direction. For the $MoS_2$ device (Figure 7A), under the 0 to 2 V forward sweep, the memristor was first located at a high-resistance state (HRS) and then switched to a low-resistance state (LRS) during the sweep. Notably, the set voltages move to smaller under light irradiation because of the additional photocurrent, indicating that light can be utilized to regulate operating voltages (Figures 7A–7E).

The asymmetric curve can be observed on the negative X axis, where the current variation is stronger than that on the positive half-axis, because of the different work functions of the top and bottom electrodes. The set voltages increase from 1.3 to 2.2 and 2.6 V with electric oxidation time from 0 s to 480 s under the bias of 3 V in Figures 7F–7I. The hysteresis tends to expand with the increase of voltage and time, which is caused by the increase of barrier height due to the formation of molybdenum oxide. According to the FNT theory, fewer

electrons are not prone to tune the barrier as the barrier increases and thus the resistance increases together with hysteresis and tends to expand. Thus, storage can be realized by applying different voltage and loading time intervals, and each local $MoS_2$-$MoO_3$ heterostructure can realize the characteristics of the multiple-state photoelectric memristor.

To further reveal the resistance regulated by voltage and loading time interval, HRS and LRS together with voltage and loading time are summarized in Table S1 and Figure S7. For HRS, the resistance increases from $1.2\times10^3$ to $3.1\times10^3$ and $4.8\times10^3$ MΩ under dark, while from $1.1\times10^3$ to $2.2\times10^3$ and $3.4\times10^3$ MΩ, respectively, after applying voltage of 0.1 and 3 V with loading time from 0 to 480 s. For LRS, the resistance increases from 20.3 to 28.9 MΩ and 18.7 to 27.5 MΩ under dark, while from 18.2 to 27.7 MΩ, and 17.4 to 27.1 MΩ under light, after respectively applying a voltage of 0.1 and 3 V with loading time from 0 to 480 s. The array of local $MoS_2$-$MoO_3$ heterostructures can induce the proposal of NanoQR code with strong encryption, consisting of a patterned multi-state photoelectric memristor as Figure 1C. The on/off ratios of our devices were estimated as 220 (Figure S8), closer to those of TMD heterojunctions of 140.[36–39] Thus, our work would provide guidelines for memory prototype of 2D $MoS_2$ photoelectric nanodevices via local electric oxidation with precisely tuning the multiple resistance at atomic scale in the information field.

### Conclusions

To summarize, the 2D $MoS_2$-$MoO_3$ local heterojunctions were constructed by local electric oxidation, which provides a new memory prototype for multistable storage. A modified thermal oxidation model was suggested to describe the relationships between the oxidation thickness and voltage, and the formation of molybdenum oxide induced by the Joule heating was identified by Raman spectra. The increase in the Schottky barrier height was caused by the formation of molybdenum oxide after the applied voltage. Multistable storage can be precisely regulated by controlling voltages and loading time together with light irradiation. This work would provide a novel design to manipulate the multistable memristors of 2D-based nanodevices and enrich thermal oxidation theory to understand the mechanism of control of oxidation thickness at the atomic level through local electric oxidation.

## RESOURCE AVAILABILITY

### Lead contact

Further information and requests for resources and materials should be directed to and will be fulfilled by the lead contact, Pro. Liang Chu (chuliang@hdu.edu.cn).

### Materials availability

The study did not generate new unique materials. The readers can buy the chemicals to remake the materials as mentioned in the text.

### Data and code availability

- Data: All data reported in this article will be shared by the lead contact upon request.
- Code: This article does not report the original code.
- Any additional information required to reanalyze the data reported in this article is available from the lead contact upon request.
- All data supporting the findings of this study are available within the article and its supplemental information or from the corresponding authors upon reasonable request.

## ACKNOWLEDGMENTS

This work was supported by the National Natural Science Foundation of China (52172205, 11832016, 51775471, 11902284, 11804166), the Natural Science Foundation of Hunan Province (2021JJ20008) and the fellowship of China postdoctoral science foundation (2021M692705).

## AUTHOR CONTRIBUTIONS

H.D conceived the idea and wrote the article. J.M and J.F.P performed AFM, SEM, TEM, and FEM calculations. X.J.Z and L. C contributed data analyses and provided instructive suggestions. All authors discussed the results and assisted in the preparation of the article.

## DECLARATION OF INTERESTS

The authors declare that they have no competing interests.

## STAR★METHODS

Detailed methods are provided in the online version of this paper and include the following:

- KEY RESOURCES TABLE
- EXPERIMENTAL MODEL AND STUDY PARTICIPANT DETAILS
- METHOD DETAILS
  - Preparation and characterization
  - Construction of $MoS_2$-based nanodevice
  - Analysis on the barrier height
  - DFT calculation method
- QUANTIFICATION AND STATISTICAL ANALYSIS
- ADDITIONAL RESOURCES

## SUPPLEMENTAL INFORMATION

Supplemental information can be found online at https://doi.org/10.1016/j.isci.2024.110819.

Received: February 7, 2024
Revised: July 6, 2024
Accepted: August 8, 2024
Published: August 31, 2024

## REFERENCES

1. Chhowalla, M., Shin, H.S., Eda, G., Li, L.-J., Loh, K.P., and Zhang, H. (2013). The chemistry of two-dimensional layered transition metal dichalcogenide nanosheets. Nat. Chem. *5*, 263–275.
2. Xiao, D., Liu, G.-B., Feng, W., Xu, X., and Yao, W. (2012). Coupled Spin and Valley Physics in Monolayers of ($MoS_2$) and Other Group-VI Dichalcogenides. Phys. Rev. Lett. *108*, 196802.
3. Spychalski, W.L., Pisarek, M., and Szoszkiewicz, R. (2017). Microscale Insight into Oxidation of Single $MoS_2$ Crystals in Air. J. Phys. Chem. C *121*, 26027–26033.
4. Yoon, A., and Lee, Z. (2017). Synthesis and Properties of Two Dimensional Doped Transition Metal Dichalcogenides. Appl. Microsc. *47*, 19–28.
5. KC, S., Longo, R.C., Wallace, R.M., and Cho, K. (2015). Surface oxidation energetics and kinetics on $MoS_2$ monolayer. J. Appl. Phys. *117*, 135301.
6. Park, W., Park, J., Jang, J., Lee, H., Jeong, H., Cho, K., Hong, S., and Lee, T. (2013). Oxygen environmental and passivation effects on molybdenum disulfide field effect transistors. Nanotechnol. *24*, 095202.
7. Chakraborty, S.K., Kundu, B., Nayak, B., Dash, S.P., and Sahoo, P.K. (2022). Challenges and opportunities in 2D heterostructures for electronic and optoelectronic devices. iScience *25*, 103942.
8. Khan, M.F., Nazir, G., Lermolenko, V.M., and Eom, J. (2016). Electrical and photo-electrical properties of $MoS_2$ nanosheets with and without an $Al_2O_3$ capping layer under various environmental conditions. Sci. Technol. Adv. Mater. *17*, 166–176.
9. Chen, J.-H., Xiong, Y.-F., Xu, F., and Lu, Y.-Q. (2021). Silica optical fiber integrated with two-dimensional materials: towards opto-electro-mechanical technology. Light Sci. Appl. *10*, 78.
10. Massoud, H.Z., Plummer, J.D., and Irene, E.A. (1985). Thermal oxidation of silicon in dry oxygen: accurate determination of the kinetic rate constants. J. Electrochem. Soc. *132*, 1745–1753.
11. Shi, Y., and Chu, L. (2023). Dipole polymer-coated crystalline grains to endure temperature variations of perovskite photovoltaics. Matter *6*, 1063–1065.
12. Yasaei, P., Hemmat, Z., Foss, C.J., Li, S.J., Hong, L., Behranginia, A., Majidi, L., Klie, R.F., Barsoum, M.W., Aksamija, Z., and Salehi-Khojin, A. (2018). Enhanced Thermal Boundary Conductance in Few-Layer $Ti_3C_2$ MXene with Encapsulation. Adv. Mater. *30*, 1801629.
13. Zein, B.E., and Habib, S.S. (2009). Small is the next big thing: thermal phenomenon on the nanoscale electronic devices. Int. J. Nanomanuf. *4*, 219–229.
14. Rao, R., Islam, A.E., Campbell, P.M., Vogel, E.M., and Maruyama, B. (2017). In situ thermal oxidation kinetics in few layer $MoS_2$. 2D Mater. *4*, 025058.
15. Kotsakidis, J.C., Zhang, Q., Vazquez de Parga, A.L., Currie, M., Helmerson, K., Gaskill, D.K., and Fuhrer, M.S. (2019). Oxidation of monolayer $WS_2$ in ambient is a photoinduced process. Nano Lett. *19*, 5205–5215.
16. Zheng, X., Wei, Y., Deng, C., Huang, H., Yu, Y., Wang, G., Peng, G., Zhu, Z., Zhang, Y., Jiang, T., et al. (2018). Controlled layer-by-layer oxidation of $MoTe_2$ via $O_3$ exposure. ACS Appl. Mater. Interfaces *10*, 30045–30050.
17. Kang, K., Godin, K., Kim, Y.D., Fu, S., Cha, W., Hone, J., and Yang, E.H. (2017). Graphene-Assisted Antioxidation of Tungsten Disulfide Monolayers: Substrate and Electric-Field Effect. Adv. Mater. *29*, 1603898.
18. Zeng, Y., He, F., Wang, Q., Yan, X., and Xie, G. (2018). Friction and wear behaviors of molybdenum disulfide nanosheets under normal electric field. Appl. Surf. Sci. *455*, 527–532.
19. Huang, P., Guo, D., Xie, G., and Li, J. (2018). Electromechanical failure of $MoS_2$ nanosheets. Phys. Chem. Chem. Phys. *20*, 18374–18379.
20. Ju, D., and Kim, S. (2024). Volatile tin oxide memristor for neuromorphic computing. iScience *27*, 110479.
21. Liu, X., Katti, K., and Jariwala, D. (2023). Accelerate and actualize: Can 2D materials bridge the gap between neuromorphic hardware and the human brain? Matter *6*, 1348–1365.
22. Kim, J.G., Liu, R., Dhakal, P., Hou, A., Gao, C., Qiu, J., Merkel, C., Zoran, M., and Wang, S. (2024). Heterostimuli chemo-modulation of neuromorphic nanocomposites for time-power-and data-efficient machine learning. Matter *7*, 1230–1244.
23. Zhai, S., Gong, J., Feng, Y., Que, Z., Mao, W., He, X., Xie, Y., Li, X., and Chu, L. (2023). Multilevel resistive switching in stable all-inorganic n-i-p double perovskite memristor. iScience *26*, 106461.
24. Sangwan, V.K., Liu, S.E., Trivedi, A.R., and Hersam, M.C. (2022). Two-dimensional materials for bio-realistic neuronal computing networks. Matter *5*, 4133–4152.
25. Lee, G.-H., Yu, Y.-J., Lee, C., Dean, C., Shepard, K.L., Kim, P., and Hone, J. (2011). Electron tunneling through atomically flat and ultrathin hexagonal boron nitride. Appl. Phys. Lett. *99*, 243114.
26. Majee, B.P., Bhawna, S.A., Prakash, R., and Mishra, A.K. (2020). Large Area Vertically Oriented Few-Layer $MoS_2$ for Efficient Thermal Conduction and Optoelectronic Applications. J. Phys. Chem. Lett. *11*, 1268–1275.
27. Hu, C., Jiang, Z., Zhou, W., Guo, M., Yu, T., Luo, X., and Yuan, C. (2019). Wafer-scale sulfur vacancy-rich monolayer $MoS_2$ for massive hydrogen production. J. Phys. Chem. Lett. *10*, 4763–4768.
28. Yamamoto, M., Einstein, T.L., Fuhrer, M.S., and Cullen, W.G. (2013). Anisotropic Etching of Atomically Thin $MoS_2$. J. Phys. Chem. C *117*, 25643–25649.
29. Windom, B.C., Sawyer, W.G., and Hahn, D.W. (2011). A Raman Spectroscopic Study of $MoS_2$ and $MoO_3$: Applications to Tribological Systems. Tribol. Lett. *42*, 301–310.
30. Diaz-Droguett, D.E., El Far, R., Fuenzalida, V.M., and Cabrera, A.L. (2012). In situ-Raman studies on thermally induced structural changes of porous $MoO_3$ prepared in vapor phase under He and $H_2$. Mater. Chem. Phys. *134*, 631–638.
31. Nicollian, E.H., and Reisman, A. (1988). A new model for the thermal oxidation kinetics of silicon. J. Electron. Mater. *17*, 263–272.
32. Laidler, K.J. (1984). The development of the Arrhenius equation. J. Chem. Educ. *61*, 494.
33. Zimmers, A., Aigouy, L., Mortier, M., Sharoni, A., Wang, S., West, K.G., Ramirez, J.G., and Schuller, I.K. (2013). Role of thermal heating on the voltage induced insulator-metal transition in $VO_2$. Phys. Rev. Lett. *110*, 056601.
34. Farmanbar, M., and Brocks, G. (2016). First-principles study of van der Waals interactions and lattice mismatch at $MoS_2$/interfaces. Phys. Rev. B *93*, 085304.
35. Lee, N., Jo, W., Liu, C., and Mény, C. (2014). Size dependent bipolar resistance switching of NiO nanodots for low-power and multi-state operation. Nanotechnology *25*, 415302.
36. Wei, X., Yan, F., Lv, Q., Shen, C., and Wang, K. (2017). Fast gate-tunable photodetection in the graphene sandwiched $WSe_2$/GaSe heterojunctions. Nanoscale *9*, 8388–8392.
37. Wei, X., Yan, F., Lv, Q., Zhu, W., Hu, C., Patanè, A., and Wang, K. (2019). Enhanced Photoresponse in $MoTe_2$ Photodetectors with Asymmetric Graphene Contacts. Adv. Opt. Mater. *7*, 1900190.
38. Wei, X., Yan, F.-G., Shen, C., Lv, Q.-S., and Wang, K.-Y. (2017). Photodetectors based on junctions of two-dimensional transition metal dichalcogenides. Chinese Phys. B *26*, 038504.
39. Lv, Q., Yan, F., Wei, X., and Wang, K. (2018). High-Performance, Self-Driven Photodetector Based on Graphene Sandwiched GaSe/WS2 Heterojunction. Adv. Opt. Mater. *6*, 1700490.
40. Foty, D.P., and Nowak, E.J. (1994). MOSFET technology for low-voltage/low-power applications. IEEE Micro *14*, 68–77.
41. Kresse, G., and Furthmüller, J. (1996). Efficiency of ab-initio total energy calculations for metals and semiconductors using a plane-wave basis set. Comput. Mater. Sci. *6*, 15–50.
42. Kresse, G., and Furthmüller, J. (1996). Efficient iterative schemes for ab initio total-energy

calculations using a plane-wave basis set. Phys. Rev. B *54*, 11169–11186.

43. Hansen, M.H., Jin, C., Thygesen, K.S., and Rossmeisl, J. (2016). Finite Bias Calculations to Model Interface Dipoles in Electrochemical Cells at the Atomic Scale. J. Phys. Chem. C *120*, 13485–13491.
44. Kresse, G., and Joubert, D. (1999). From ultrasoft pseudopotentials to the projector augmented-wave method. Phys. Rev. B *59*, 1758–1775.
45. Blöchl, P.E. (1994). Projector augmented-wave method. Phys. Rev. B *50*, 17953–17979.
46. Perdew, J.P., Burke, K., and Ernzerhof, M. (1996). Generalized gradient approximation made simple. Phys. Rev. Lett. *77*, 3865–3868.
47. Bucko, T., Hafner, J., Lebegue, S., and Angyán, J.G. (2010). Improved description of the structure of molecular and layered crystals: ab initio DFT calculations with van der Waals corrections. J. Phys. Chem. A *114*, 11814–11824.
48. Grimme, S. (2006). Semiempirical GGA-type density functional constructed with a long-range dispersion correction. J. Comput. Chem. *27*, 1787–1799.

# STAR★METHODS

## KEY RESOURCES TABLE

| REAGENT or RESOURCE | SOURCE | IDENTIFIER |
|---|---|---|
| Chemicals, peptides, and recombinant proteins | | |
| $Mos_2$ single crystal | Nanjing MKNANO Technology Co., Ltd | N/A |
| Pt substate | Nanjing MKNANO Technology Co., Ltd | N/A |

## EXPERIMENTAL MODEL AND STUDY PARTICIPANT DETAILS

There are no experimental models (animals, human subjects, plants, microbe strains, cell lines, primary cell cultures) used in the study.

## METHOD DETAILS

### Preparation and characterization

$MoS_2$ single crystal and Pt-coated $SiO_2$/Si(100) substrate were purchased from Nanjing MKNANO Technology Co., Ltd. The $MoS_2$ single-crystal 2D nanosheets were prepared by ultrahigh-pressure and low-temperature exfoliation of our unpublished method and then transferred to the above substrate. The crystalline structure and surface morphology were characterized by X-ray diffraction (XRD, Bruker, D8 Advance Cu-Ka, German), scanning electron microscope (SEM, Hitachi, SU5000, Japan), atomic force microscopy (AFM, Cypher S, Oxford Instruments, USA), and high-resolution transmission electron microscope (HRTEM, Titan, 80–300 kV, USA).

### Construction of $MoS_2$-based nanodevice

The $MoS_2$-based nanodevices were constructed using conductive AFM with architecture of Au tip/$MoS_2$ nanosheet/Pt substrate. The different interval voltages were applied on the local nanodevices. The photoelectric properties of nanodevices were measured under light irradiation, when Au-coated Si tip (PPP-NCHAu) was always grounded. Power consumption is a major concern because of the ever-increasing density of solid-state electronic devices, and it is known that power consumption drops quadratically with decrease of supply voltage.[40] Under the high and low supply voltages the power consumption may be differently varied, therefore the high voltages of 3, 4, and 5 V and low voltages of 0.1, 0.3, and 0.5 V were applied at the different points for the loading time interval 30 s and 480 s. The voltages of 0.1–5 V were applied on the $MoS_2$ nanosheets with the loading time intervals of 0–480 s, before the *I-V* and current-time (*I-t*) characteristics were measured by sweeping voltage from −3 V to +4 V and applying a voltage of 0.5 V under the dark condition and laser irradiation (660 nm, 2 mW/cm$^2$). The light was only applied for sweeping voltage from −3 V to +4 V as comparison with those under the dark conditions not through the whole measurement process. Raman spectra of $MoS_2$ nanosheet at pristine and after the applied voltage 5 V were carried out using Raman microscope (Raman, InVia Raman Microscope, Renishaw, UK) at a wavelength of 532 nm, so that the phase formation of molybdenum oxide could be identified by the enlarged peaks with main Raman active modes. The oxidation thickness was determined by comparing height profiles of $MoS_2$ nanosheet at pristine and after the applied voltage states.

### Analysis on the barrier height

Based on the FNT theory, the equivalent barrier height $\phi_e$ could be analyzed by *I-V* characteristics[25]:

$$I(V) = \frac{A_{eff} q^3 m V^2}{8\pi h \phi_e d^2 m^*} \exp\left(\frac{-8\pi\sqrt{2m^*}\phi_e^{\frac{3}{2}} d}{3hqV}\right) \quad \text{(Equation 5)}$$

where $\phi_e$, $A_{eff}$, $q$, $m$, $m^*$, $d$, and $h$ are the barrier height, the effective contact area, electron charge, free electron mass, effective electron mass separation between two electrodes, the distance between two electrodes, and Planck's constant, respectively. $A_{eff}$ could be estimated by circular contact area with the diameter of AFM tip. For line fitting of *I-V* curves, the Equation 1 can be expressed as follows:

$$\ln\frac{I(V)}{V^2} = \ln\frac{A_{eff} q^3 m}{8\pi h \phi_e d^2 m^*} - \frac{8\pi\sqrt{2m^*}\phi_e^{\frac{3}{2}} d}{3hqV} \quad \text{(Equation 6)}$$

$\phi_e$ could be obtained by fitting the $\ln(I/V^2)$ versus $1/V$ curves through linear fitting method, therefore it can be determined that the barrier height difference $\Delta\phi_e$ between $MoS_2$ nanosheet at pristine and after the applied voltages.

### DFT calculation method

The electrostatic potentials of $MoS_2$ and $MoS_2$-$MoO_3$ layers were calculated by using Vienna Ab-initio Simulation Package (VASP),[41,42] as the stable energy level on the electrostatic potential is generally defined as the vacuum level.[43] The difference in Schottky barrier height $\Delta\phi$ ($\phi_1-\phi_2$) would be calculated for the heterostructures at pristine states and after the applied voltage, and they are compared with the barrier height difference $\Delta\phi_e$ to analyze the variation on tunneling current. The projector-augmented wave method was applied to describe electron-ion interactions,[44,45] whereas the exchange-correlation function was treated by the generalized gradient approximation considering Perdew-Burke-Ernzerhof method.[46] van der Waals corrections were included by using Grimmes DFT-D2 method as implemented in VASP.[47,48] The cutoff energy of the plane wave was set to 400 eV, and the atomic positions were fully relaxed until the maximum force less than 0.01 $eV^{-1}$ on each atom. *K*-point samplings of 3 × 3 × 1 and 3 × 3 × 1 were used for $MoS_2$ and $MoS_2$-$MoO_3$ heterostructures, and a vacuum region of 15 Å was introduced to avoid any spurious interactions. Electrostatic potentials and band structures were carried out to study the barrier height difference at the certain points on $MoS_2$ and $MoS_2$-$MoO_3$ supercells. The Schottky barrier height $\phi$ of electrons is defined as follows[34]:

$$\phi = W_{Au} - \chi \quad \text{(Equation 7)}$$

$$\chi = E_0 - E_c \quad \text{(Equation 8)}$$

where $W_{Au}$ is the work function of gold, $\chi$ is the electron affinity of the semiconductor, $E_0$ is the vacuum level, and $E_c$ is the minimum conduction band.

## QUANTIFICATION AND STATISTICAL ANALYSIS

This study does not include statistical analysis or quantification.

## ADDITIONAL RESOURCES

This work does not include any additional resource.